Tracking Control with Adjustable Trajectory Envelope for Cable-Driven Robots

Haining Sun, Rongqiao Zhang, Ruihang Ji, Xiaoqiang Tang, and Shuzhi Sam Ge, *Fellow, IEEE*

***Abstract*—In industrial applications, insufficient motor torque and overload issues can limit the control force in cable-driven robots (CDRs), affecting the stability and robustness of trajectory tracking control. This work presents a specialized tracking controller to achieve stable trajectory tracking under constrained control forces. The controller incorporates a trajectory envelope system that actively adjusts the permissible range of the actual trajectory. When control forces approach their upper limits, the envelope automatically expands and reduces the precision requirement for trajectory tracking. The controller then ensures that the actual trajectory remains within the designated permissible boundaries, thereby maintaining controllable trajectory tracking. The stability of the control system is validated using the Lyapunov method. Experimental validations on CDRs with one, two, and four cables are conducted. Both simulations and experiments confirm the effectiveness of the proposed tracking controller under conditions of constrained motor output torque.**

***Index Terms*—Cable-driven robots, tracking control, constrained control force.**

I. INTRODUCTION

Cable-driven robots (CDRs) combine a large workspace, low inertia and excellent payload capacity. Numerous studies have confirmed their great potential for industrial applications, such as recovery and rescue [1], vibration suppression for rigid and flexible structures [2-4], cargo grabbing [5], [6], facade cleaning [7], surgery [8], as well as warehouse monitoring [9]. Importantly, all these applications rely on trajectory tracking control. Starting with the widely-used model-free PID control [10], many tracking methods have been proposed, including intelligent PID control [11], cascade control [12], and vision-based tracking control [13]. However, focusing solely on reducing tracking errors is no longer sufficient to meet the diverse needs of control systems in practical applications. Therefore, current controllers take into consideration a broader range of factors, including convergence speed [14], cable synchronization [15-17], trajectory smoothness [18-20], uncertainty compensation [21], [22], and vibration elimination [23], [24].

Despite these advances, a critical issue in tracking control of CDRs remains unresolved: achieving controllable tracking under constrained control forces. It is important to note that insufficient motor torque or excessive load can cause the actual control forces to reach their upper limits, leading to unpredictable trajectories that differ from expectations, thereby increasing tracking errors and potentially destabilizing the controller. Simulations in [25] demonstrated that large tracking errors could result in tracking failure under constrained control inputs. Moreover, experiments conducted in [26] showed that when the control force reached its upper limit, it severely disrupted trajectory tracking. Although these studies did not quantitatively analyze the relationship between the constrained control inputs and trajectory tracking, they highlighted the existence of this problem and the importance of ensuring controllable motion when the control force reaches the upper limit during trajectory tracking.

Limited research has focused on addressing the issue of constrained control force in trajectory tracking for CDRs. For example, a bounded adaptive trajectory tracking controller was introduced in [27], which combined a PD controller with adaptive feedback and constrained the output of the PD controller. Notably, this approach limited only the lower bound of the control force while neglecting any constraints on the upper limit. A force distribution technique was introduced in [28] to constrain the lower limit of the control force to ensure positive cable tension. However, the cases where control inputs reach their upper limit are not studied. Similarly, in [29], only the case of limiting the lower limit of the actual control force was studied. While the controller in [30] had an upper limit on the control force, it regulated the cable force within a specified range to prevent reaching the upper limit or set an upper limit higher than the actual control force. A similar approach was adopted in [31] to prevent the initial observation errors from causing the control input to reach the upper limit. It compensated for these errors at the outset to keep the actual cable force below the upper limit. Although the above studies

Manuscript received April xx, 2024. This work was supported in part by the National Natural Science Foundation of China under Grant 51975307 and the Ministry of Education, Singapore, under its Research Centre of Excellence award to the Institute for Functional Intelligent Materials (I-FIM, project No. EDUNC-33-18-279-V12). (Corresponding author: X. Tang and S. S. Ge).

H. Sun is with the Department of Mechanical Engineering, Tsinghua University, Beijing, 100084, China, and also with Singapore Institute of Manufacturing Technology, A*STAR, 138634, Singapore (e-mail: sunhn@simtech. a-star.edu.sg).

R. Zhang and X. Tang are with State Key Laboratory of Tribology, Department of Mechanical Engineering, Tsinghua University, Beijing, 100084, China (e-mail: tang-xq@mail.tsinghua.edu.cn; zrq21@mails.tsinghua.edu.cn).

R. Ji and S. S. Ge are with the Department of Electrical and Computer Engineering, and Institute for Functional Intelligent Materials, National University of Singapore, Singapore 117583 (e-mail: jiruihang@nus.edu.sg; samge@nus.edu.sg).

introduced the concept of constrained control force, they mainly focused on setting the lower limit and did not explore the stability of tracking controllers when the control input reached the upper limit.

Most studies [14-31] on the cable force control of CDRs have a common premise: the output torque of the motor will not reach an upper limit during operation. This premise holds true in laboratory environments, where power supplies are stable and sufficiently robust to prevent any drop in motor torque due to voltage fluctuations. However, outdoor applications such as solar panel cleaning or facade maintenance present a challenge. In these applications, robots are typically powered by batteries, which inevitably leads to decreases in supply voltage as the batteries discharge. For example, a fully charged 24 V lithium battery can experience a voltage drop to 18 V as it discharges, resulting in reduced motor torque that prevents the motor from maintaining normal output levels. This situation highlights the necessity for stable motion control strategies that can adapt to constrained control inputs, especially when the motor torque reaches its upper limit.

Moreover, ensuring controllable motion is more challenging when an upper limit is set on motor torque than when a lower limit is set. For fully constrained CDRs, setting a lower limit can ensure that the cables remain in tension, which is beneficial for improving the stiffness of CDRs and ensuring accurate trajectory tracking. However, imposing an upper limit may cause the actual torque to fail to reach the target torque. This deviation can cause the robot's actual trajectory to diverge from the target trajectory, increasing the risk of operational failures or even loss of control. This problem was examined in [25] and [26], which demonstrated that reaching the upper limits of control inputs can cause failures in trajectory tracking. To address this problem, several novel controllers were proposed in [32-35]. For example, a flexible performance-based control scheme was proposed in [34] to handle constrained inputs, which included a disturbance observer to estimate external disturbances. A fuzzy state observer was further introduced to estimate system states under input saturation and actuator faults in [35]. Simulations validated the effectiveness of these controllers. Their practical effectiveness has not been validated in experiments, especially for redundant CDRs. Our work aims to develop a tracking controller for redundant CDRs to ensure stable motion even when the control inputs reach their limits, while also being practically feasible.

The contributions of this study are as follows:

(1) Compared to [27-31], our work introduces a trajectory envelope generator that quantitatively links limited control input to the permissible range of the actual trajectory. The generator actively adjusts this range, shifting the control objective from accurately tracking the target trajectory to maintaining the actual trajectory within this range.

(2) The designed tracking controller ensures that the actual trajectory remains within the specified allowable range even when control inputs reach the upper limits. Compared to the commonly used model predictive control in [25] and [36], the proposed controller achieves faster convergence to the target trajectory under constrained control inputs.

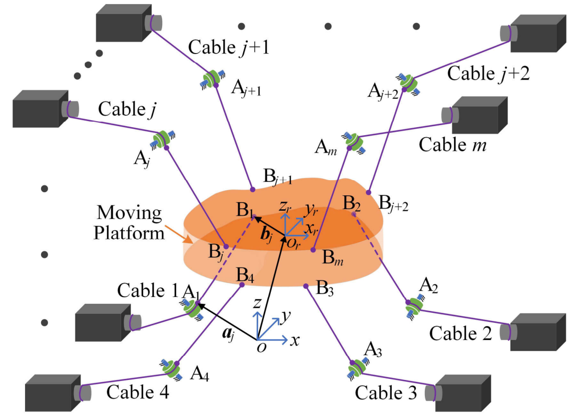

Fig. 1. A m-cable cable-driven robot.

(3) Experiments are conducted on a CDR with three configurations: one cable, two cables, and four cables. The results verify that the controller maintains stable trajectory tracking even with a tracking error of up to 0.89 m. It effectively broadens the trajectory envelope to consistently encompass the actual trajectory, ensuring controllable trajectory tracking without mid-course failures.

In the subsequent sections, Section II introduces the dynamic model of the CDR. Section III details the design of the tracking controller. Simulation and experiments are conducted in Section IV, while the work is concluded in Section V.

II. Dynamic Model

This part introduces the dynamic model of a m-cable CDR (Fig. 1). The moving platform is linked to cable j at B_j, and the mass of cables is ignored. The Cable j is connected to the winch via the fixed anchor point A_j. $\{o\}$ is the reference coordinate frame. $\{o_r\}$ is the moving coordinate frame fixed on the moving platform. The CDRs' kinematic model is described as:

$$\boldsymbol{p} = \boldsymbol{a}_j - \boldsymbol{l}_j - {}^{o}\boldsymbol{R}_{o_r}\boldsymbol{b}_j \quad (j = 1,2,...,m) \tag{1}$$

where $\boldsymbol{l}_j$ represents the cable vector pointing from B_j to A_j, $\boldsymbol{a}_j$ is the vector pointing from o to A_j, $\boldsymbol{p} = [x_p, y_p, z_p]^T$ denotes the position of $\{o_r\}$ in $\{o\}$, ${}^{o}\boldsymbol{R}_{o_r}$ is the rotation matrix, $\boldsymbol{b}_j$ is the vector pointing from o_r to B_j in $\{o_r\}$.

The dynamic model of the CDR can be expressed as follows:

$$\boldsymbol{M}(\boldsymbol{x})\ddot{\boldsymbol{x}} + \boldsymbol{C}(\boldsymbol{x},\dot{\boldsymbol{x}})\dot{\boldsymbol{x}} + \boldsymbol{G}(\boldsymbol{x}) = -\boldsymbol{J}^T\boldsymbol{F} \tag{2}$$

where the inertia matrix $\boldsymbol{M}(\boldsymbol{x})$, the Coriolis and centrifugal matrix $\boldsymbol{C}(\boldsymbol{x},\dot{\boldsymbol{x}})$, and the Jacobian matrix $\boldsymbol{J}$ are expressed as:

$$\boldsymbol{M}(\boldsymbol{x}) = \begin{bmatrix} m_r\boldsymbol{I}_{3\times3} & \boldsymbol{0}_{3\times3} \\ \boldsymbol{0}_{3\times3} & \boldsymbol{E}^T\boldsymbol{I}_r\boldsymbol{E} \end{bmatrix} \tag{3}$$

$$\boldsymbol{C}(\boldsymbol{x},\dot{\boldsymbol{x}}) = \begin{bmatrix} \boldsymbol{0}_{3\times3} & \boldsymbol{0}_{3\times3} \\ \boldsymbol{0}_{3\times3} & \boldsymbol{E}^T\boldsymbol{E}_\theta\boldsymbol{I}_r\boldsymbol{E} + \boldsymbol{E}^T\boldsymbol{I}_r\dot{\boldsymbol{E}} \end{bmatrix} \tag{4}$$

$$\boldsymbol{J} = \begin{bmatrix} \boldsymbol{r}_1 & \cdots & \boldsymbol{r}_m \\ {}^{o}\boldsymbol{R}_{o_r}\boldsymbol{b}_1\times\boldsymbol{r}_1 & \cdots & {}^{o}\boldsymbol{R}_{o_r}\boldsymbol{b}_m\times\boldsymbol{r}_m \end{bmatrix}^T \begin{bmatrix} \boldsymbol{I}_{3\times3} & \boldsymbol{0}_{3\times3} \\ \boldsymbol{0}_{3\times3} & \boldsymbol{E} \end{bmatrix} \tag{5}$$

The gravity item $\boldsymbol{G}(\boldsymbol{x}) = [m_r\boldsymbol{g}, \boldsymbol{T}_r]^T$ has $\boldsymbol{g} = [0, 0, -9.8]$ m/s^2 and $\boldsymbol{T}_r = [0, 0, 0]$ Nm. The posture is $\boldsymbol{x} = [\boldsymbol{p}, \boldsymbol{\theta}]^T = [x_p, y_p, z_p, \alpha, \beta, \varsigma]^T$. Cable forces are $\boldsymbol{F} = [F_1, \ldots, F_m]^T$. m_r and $\boldsymbol{I}_r$ respectively denote the mass and inertia matrix. $\boldsymbol{\theta} = [\alpha, \beta, \varsigma]^T$ denotes Euler angles.

$\boldsymbol{r}_j = \boldsymbol{l}_j / l_j$, where $l_j = \sqrt{[\boldsymbol{a}_j - \boldsymbol{p} - {}^{O}\boldsymbol{R}_{O_r}\boldsymbol{b}_j]^T \cdot [\boldsymbol{a}_j - \boldsymbol{p} - {}^{O}\boldsymbol{R}_{O_r}\boldsymbol{b}_j]}$ is the unit vector along the j-th cable. Let symbol $c(\cdot) = \cos(\cdot)$ and $s(\cdot) = \sin(\cdot)$, we obtain:

$$\boldsymbol{E} = \begin{bmatrix} c\beta c\varsigma & -s\varsigma & 0 \\ c\beta s\varsigma & c\varsigma & 0 \\ -s\beta & 0 & 1 \end{bmatrix} \tag{6}$$

$$\boldsymbol{E}_\theta = \begin{bmatrix} 0 & s\beta\dot{\alpha} - \dot{\varsigma} & c\beta s\varsigma\dot{\alpha} + c\varsigma\dot{\beta} \\ -s\beta\dot{\alpha} + \dot{\varsigma} & 0 & -c\beta c\varsigma\dot{\alpha} + s\varsigma\dot{\beta} \\ -c\beta s\varsigma\dot{\alpha} - c\varsigma\dot{\beta} & c\beta c\varsigma\dot{\alpha} - s\varsigma\dot{\beta} & 0 \end{bmatrix} \tag{7}$$

By defining $\boldsymbol{x}_1 = \boldsymbol{x}$, $\boldsymbol{x}_2 = \dot{\boldsymbol{x}}$, we can rewrite (2) as follows:

$$\begin{cases} \dot{\boldsymbol{x}}_1 = \boldsymbol{x}_2 \\ \dot{\boldsymbol{x}}_2 = \left(\boldsymbol{M}(\boldsymbol{x})\right)^{-1}\left(-\boldsymbol{J}^T\boldsymbol{F} - \boldsymbol{G}(\boldsymbol{x}) - \boldsymbol{C}(\boldsymbol{x}, \dot{\boldsymbol{x}})\dot{\boldsymbol{x}}\right) \end{cases} \tag{8}$$

Let k ($k = 1, \ldots, 6$) represent each element $(x_p, y_p, z_p, \alpha, \beta, \varsigma)$ in $\boldsymbol{x}_1$, we can convert (8) into:

$$\begin{cases} \dot{x}_{k,1} = x_{k,2} \\ \dot{x}_{k,2} = \underbrace{-\left(\left(\boldsymbol{M}(\boldsymbol{x})\right)^{-1}\boldsymbol{J}^T\boldsymbol{F}\right)_k}_{v_k} \underbrace{-\left(\left(\boldsymbol{M}(\boldsymbol{x})\right)^{-1}\left(\boldsymbol{G}(\boldsymbol{x}) + \boldsymbol{C}(\boldsymbol{x}, \dot{\boldsymbol{x}})\dot{\boldsymbol{x}}\right)\right)_k}_{f_{k,2}(\boldsymbol{x})} \end{cases} \tag{9}$$

$$v_k(u_k) = \begin{cases} u_{\max,k}, & \text{if } u_k > u_{\max,k} \\ u_k, & \text{if } u_{\min,k} \le u_k \le u_{\max,k} \\ u_{\min,k}, & \text{if } u_k < u_{\min,k} \end{cases} \tag{10}$$

where $f_{k,2}$ is a continuous function defined in (9). v_k denotes the actual control input that suffers from the saturation constraint in (10). This constraint on v_k is converted into a constraint on $\boldsymbol{F}$ by (9). Therefore, both v_k and $\boldsymbol{F}$ are constrained. The purpose of replacing $\boldsymbol{F}$ with v_k in this manner is to simplify the complexity of the derivation. The notation $(\cdot)_k$ denotes the k-th element of the vector in the bracket. $u_{\max,k}$ and $u_{\min,k}$ are given constants. u_k is the desired control input to be designed in this work. Based on u_k, and in combination with (9) and (10), we obtain v_k and $\boldsymbol{F}$.

Remark 1: According to [11], [12], [16], [25], and [28], the inertia matrix $\boldsymbol{M}(\boldsymbol{x})$ is a positive definite matrix in CDRs, which is invertible. For the Jacobian matrix $\boldsymbol{J}$ in CDRs, its Moore–Penrose inverse is commonly used in calculations.

III. Controller Design

To proceed with the design of the controller, we introduce the following assumption. The rationale of this assumption is explained in detail in [39]. It is also verified in [41] that feasible control inputs exist in the case of input saturation.

Assumption 1 [39]: For a practical system described by (9) subject to constrained inputs (10), there should exist a feasible control input to achieve stable trajectory tracking control.

A. Trajectory envelope generator

Generally, the tracking error is expected to remain within a narrow range close to zero, as shown in Fig. 2(a) and (11).

$$-\alpha_k^- \le \varphi_k \le \alpha_k^+ \tag{11}$$

where α_k^- and α_k^+ ($k = 1, 2, \ldots, 6$) are positive scalars. Denoting $\boldsymbol{x}_d = [x_{d1}, x_{d2}, x_{d3}, x_{d4}, x_{d5}, x_{d6}]^T$ as the target trajectory and $\boldsymbol{\varphi} = \boldsymbol{x}_1 - \boldsymbol{x}_d = [\varphi_1, \ldots \varphi_k, \ldots, \varphi_6]^T$ as the tracking error.

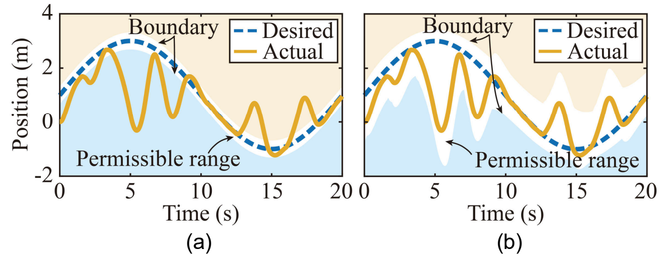

Fig. 2. Boundary for actual trajectory. (a) General allowed range for actual trajectory. (b) Adjustable range for actual trajectory.

When the control input reaches its upper limit, the actual trajectory will deviate from the target trajectory. Since the control input is already at its maximum, it's difficult to correct the deviation of the actual trajectory from the target trajectory. The constrained control input and increasing tracking errors poses a risk of losing control, as mentioned in [25].

A feasible solution is to widen the allowable range in (11) for the actual trajectory and adjust it based on the constraints on the control input. Although the actual trajectory deviates from the target trajectory when control inputs are limited, we can keep it within a variable allowable range. Therefore, the controller's objective shifts from accurately tracking the target trajectory to maintaining the actual trajectory within the specified range, which avoids the continuous increase of control input. With this concept, we can reformulate (11) as follows:

$$\varphi_{g,k}^- \le \varphi_k \le \varphi_{g,k}^+ \tag{12}$$

Different from α_k^- and α_k^+, $\varphi_{g,k}^-$ and $\varphi_{g,k}^+$ are two variables that vary based on the constrained control input and tracking errors. $\varphi_{g,k}^-$ ($\varphi_{g,k}^+$) consists of two parts. The first part is the inherent envelope φ_k^- (φ_k^+), which makes the actual trajectory gradually converge to the target trajectory, as shown in (13).

$$\varphi_k^- = \varphi_k^+ = \beta_{k,Amp} e^{-\xi t} + \beta_{k,bias} \tag{13}$$

where $\beta_{k,Amp}$, $\beta_{k,bias}$, and ξ are positive scalars.

The second part is the variable envelope $g_{k,1}^-$ and $g_{k,1}^+$, which actively expands the allowable range when the control input v_k is limited. Let' introduce a series of intermediate variables $g_{k,2}^-, \ldots, g_{k,n}^-, g_{k,2}^+, \ldots, g_{k,n}^+$, which have no physical meaning and are solely used to solve the variable envelopes $g_{k,1}^-$ and $g_{k,1}^+$, as shown in (14) and (15). $\lambda_1^-, \ldots, \lambda_n^-, \lambda_1^+, \ldots, \lambda_n^+$ are a series of control parameters (positive constants). n denotes the order of the model (9). The subscript i denotes the index of a variable or a parameter in a sequence. For example, in $g_{k,i}^-$, i indicates that $g_{k,i}^-$ is the i-th variable among $g_{k,1}^-, \ldots, g_{k,n}^-$.

For $\varphi_{g,k}^-$, the lower variable envelope is designed as follows:

$$\begin{aligned} \dot{g}_{k,1}^- &= \left(\partial z_{k,1}/\partial \varphi_{g,k}^-\right)^{-1}\left(\partial z_{k,1}/\partial \varphi_k\right)\left(-\lambda_1^- g_{k,1}^- + g_{k,2}^-\right) \\ \dot{g}_{k,i}^- &= -\lambda_i^- g_{k,i}^- + g_{k,i+1}^- \quad i = 2, \ldots, n \end{aligned} \tag{14}$$

For $\varphi_{g,k}^+$, the upper variable envelope is designed as follows:

$$\begin{aligned} \dot{g}_{k,1}^+ &= -\left(\partial z_{k,1}/\partial \varphi_{g,k}^+\right)^{-1}\left(\partial z_{k,1}/\partial \varphi_k\right)\left(-\lambda_1^+ g_{k,1}^+ + g_{k,2}^+\right) \\ \dot{g}_{k,i}^+ &= -\lambda_i^+ g_{k,i}^+ + g_{k,i+1}^+ \quad i = 2, \ldots, n \end{aligned} \tag{15}$$

where $g_{k,1}^+(0) = g_{k,1}^-(0) = g_{k,i}^+(0) = g_{k,i}^-(0) = 0$. $g_{k,n+1}^-$ denotes the difference between the desired control input u_k and the actual control input v_k after reaching the upper limit, and $g_{k,n+1}^{+}$ is the difference between u_k and v_k after reaching the lower limit:

$$\begin{cases} g_{k,n+1}^{-} = u_k - v_k\left(u_k\right), \text{ if } u_k - v_k\left(u_k\right) \ge 0 \\ g_{k,n+1}^{+} = v_k\left(u_k\right) - u_k, \text{ if } u_k - v_k\left(u_k\right) \le 0 \\ g_{k,n+1}^{+} = g_{k,n+1}^{-} = 0, \quad \text{others} \end{cases} \tag{16}$$

Let's introduce an intermediate variable $z_{k,1}$, and define its relationship with the tracking error φ_k as follows:

$$\varphi_k = \frac{\varphi_{g,k}^{+} + \varphi_{g,k}^{-}}{2}\left(\frac{2}{\pi}\arctan\left(z_{k,1}\right)\right) + \frac{\varphi_{g,k}^{+} - \varphi_{g,k}^{-}}{2} \tag{17}$$

Based on (12) to (17), the trajectory envelope generator can be expressed as follows:

$$-\underbrace{\left(\varphi_k^{-} + g_{k,1}^{-}\right)}_{\varphi_{g,k}^{-}} < \varphi_k < \underbrace{\varphi_k^{+} + g_{k,1}^{+}}_{\varphi_{g,k}^{+}} \tag{18}$$

In (17), $z_{k,1}$ can be considered as a function with φ_k, $\varphi_{g,k}^{+}$, and $\varphi_{g,k}^{-}$ as its three variables. Symbolic function operations in MATLAB can be used to obtain the partial derivatives in (14) and (15). To prove that these partial derivatives ((A.1)-(A.3) in the appendix) are non-zero, we introduce the following lemma.

Lemma 1 [37]: Consider $\dot{\boldsymbol{y}}(t) = \boldsymbol{K}\boldsymbol{y}(t) + \boldsymbol{d}(t)$ with $\boldsymbol{K}$ being a $n\times n$ Metzler matrix (i.e., off-diagonal terms are nonnegative), $\boldsymbol{y}(t) = [y_1(t), \ldots, y_n(t)]^T$, and $\boldsymbol{d}(t) = [d_1(t), \ldots, d_n(t)]^T$, where $\boldsymbol{d}(t) \ge 0$. Then, for any $\boldsymbol{y}(0) \ge 0$, the unique solution of the system has $\boldsymbol{y}(t) \ge 0$ for all $t \ge 0$. Here, $\boldsymbol{d}(t) \ge 0$ denotes that any element $d_i(t)$ in $\boldsymbol{d}(t)$ satisfies $d_i(t) \ge 0$, and $\boldsymbol{y}(t) \ge 0$ denotes that any element $y_i(t)$ in $\boldsymbol{y}(t)$ satisfies $y_i(t) \ge 0$ ($i = 1, \ldots, n$).

Remark 2: Considering the initial conditions $g_{k,1}^{+}(0) = g_{k,1}^{-}(0) = g_{k,i}^{+}(0) = g_{k,i}^{-}(0) = 0$, and combining *Lemma 1* with (16), we obtain that the variable envelopes defined in (14) and (15) satisfy $g_{k,1}^{-} \ge 0$ and $g_{k,1}^{+} \ge 0$. Furthermore, in combination with (13), it is evident that the envelopes $\varphi_{g,k}^{+} > 0$ and $\varphi_{g,k}^{-} > 0$. Then, based on the partial derivatives (A.1)-(A.3) in the appendix, it can be concluded that they are always non-zero.

According to (14)-(16), we can conclude that for any given positive constant u_c, if the inequality $|u_k - v_k(u_k)| \le u_c$ and (18) hold for $t \ge 0$, then $g_{k,1}^{-} \le u_c\Pi_{i=1}^{n}(\lambda_i^{-})^{-1}$ and $g_{k,1}^{+} \le u_c\Pi_{i=1}^{n}(\lambda_i^{+})^{-1}$. Combining *Lemma 1* with (16), we have $g_{k,n}^{-} \ge 0$ and $g_{k,n}^{+} \ge 0$. If $g_{k,n}^{-} > (\lambda_n^{-})^{-1}u_c$, we can obtain $\dot{g}_{k,n}^{-} < 0$ based on (14), which indicates that $0 \le g_{k,n}^{-} \le (\lambda_n^{-})^{-1}u_c$. Similarly, we can also obtain $0 \le g_{k,n}^{+} \le (\lambda_n^{+})^{-1}u_c$. Then, we can inductively obtain that $0 \le g_{k,2}^{-} \le u_c\Pi_{i=2}^{n}(\lambda_i^{-})^{-1}$ and $0 \le g_{k,2}^{+} \le u_c\Pi_{i=2}^{n}(\lambda_i^{+})^{-1}$. Likewise, we can obtain $g_{k,1}^{-} \le u_c\Pi_{i=1}^{n}(\lambda_i^{-})^{-1}$ and $g_{k,1}^{+} \le u_c\Pi_{i=1}^{n}(\lambda_i^{+})^{-1}$. By combining *Remark 2*, we finally have $0 \le g_{k,1}^{-} \le u_c\Pi_{i=1}^{n}(\lambda_i^{-})^{-1}$ and $0 \le g_{k,1}^{+} \le u_c\Pi_{i=1}^{n}(\lambda_i^{+})^{-1}$.

B. Tracking controller

Firstly, we introduce a series of intermediate variables, denoted as $z_{k,i}$, where k ($k = 1, 2, \ldots, 6$) represents each element $x_p, y_p, z_p, \alpha, \beta, \varsigma$ in $\boldsymbol{x}_1$, and i ($i = 1, 2, \ldots$) is the sequence number. For example, $z_{2,2}$ denotes the second intermediate variable for the degree of freedom y_p. These intermediate variables have no physical significance. We simply use them to replace lengthy addition and subtraction terms involving multiple variables to further simplify the equations and facilitate the derivation.

Theorem 1: Consider the following control input:

$$\begin{cases} \bar{u}_{k,1} = \dot{x}_{dk} - \left(\partial_k^{z\varphi}\right)^{-1}\left(\partial_k^{z\varphi^{+}}\dot{\varphi}_k^{+} + \partial_k^{z\varphi^{-}}\dot{\varphi}_k^{-}\right) - \left(\lambda_1^{+}g_{k,1}^{+} - \lambda_1^{-}g_{k,1}^{-}\right) \\ \qquad -\left(\partial_k^{z\varphi}\right)^{-1}\left(\delta_{k,1}z_{k,1} + \sigma_{k,1}sign(z_{k,1})\left|z_{k,1}\right|^{\gamma}\right) \\ u_k = -\left(\lambda_2^{+}g_{k,2}^{+} - \lambda_2^{-}g_{k,2}^{-}\right) - z_{k,1}\partial_k^{z\varphi} + \dot{\omega}_{k,2} \\ \qquad -\left(\delta_{k,2}z_{k,2} + \sigma_{k,2}sign(z_{k,2})\left|z_{k,2}\right|^{\gamma}\right) \end{cases} \tag{19}$$

where:

$$\partial_k^{z\varphi} = \partial z_{k,1}/\partial\varphi_k, \partial_k^{z\varphi^{+}} = \partial z_{k,1}/\partial\varphi_{g,k}^{+}, \partial_k^{z\varphi^{-}} = \partial z_{k,1}/\partial\varphi_{g,k}^{-} \tag{20}$$

where intermediate variables $z_{k,1}$ and $z_{k,2}$ are shown in (17) and (A.10), respectively. The definition of $\omega_{k,2}$ is shown in (A.8). There exist positive parameters $\delta_{k,i}$, λ_i^{+}, λ_i^{-}, $\sigma_{k,i}$, γ, and $\varepsilon_{k,2}$ ($i = 1, 2$) ensuring that the system states of the closed-loop system are uniformly bounded.

Proof: The selection of the Lyapunov candidate functions and calculation process are detailed in the appendix. Following the stability proof method in [38], we will define several compact sets. Let's introduce positive constants M_Y and M_Z. Define three vectors: $\boldsymbol{Y} = [x_{dk}, \dot{x}_{dk}, \ddot{x}_{dk}]^T$, $\boldsymbol{Z} = [z_{k,1}, z_{k,2}, \phi_{k,2}]^T$, and $\boldsymbol{G} = [g_{k,1}^{-}, g_{k,2}^{-}, g_{k,1}^{+}, g_{k,2}^{+}]^T$. Define $\bar{g}_i = \Pi_i^2(\lambda_i^{-})^{-1} = \Pi_i^2(\lambda_i^{+})^{-1}$, where $i = 1, 2$ and $\lambda_i^{-} = \lambda_i^{+}$. Consider sets: $Q_1 := \{\boldsymbol{Y} : \|\boldsymbol{Y}\|^2 \le M_Y\}$, $Q_2 := \{\boldsymbol{Z} : \|\boldsymbol{Z}\|^2 \le 2M_Z\}$, and $Q_3 := \{\boldsymbol{G} : 0 \le g_{k,i}^{-}, g_{k,i}^{+} \le \bar{g}_i u_c\}$ with $i = 1, 2$. The three sets Q_1, Q_2, and Q_3 are compact sets. Therefore, $Q_4 = Q_1 \times Q_2 \times Q_3$ is also compact in $\mathbb{R}^{10}$. Within the compact set Q_4, there exists a positive constant M_f such that $f_{k,2}^2(\boldsymbol{x}) \le M_f$. Moreover, the derivative of the virtual control input $\bar{u}_{k,1}$ is expressed as follows:

$$\begin{aligned} \dot{\bar{u}}_{k,1} = &\frac{\partial\bar{u}_{k,1}}{\partial x_{dk}}\dot{x}_{dk} + \frac{\partial\bar{u}_{k,1}}{\partial\dot{x}_{dk}}\ddot{x}_{dk} + \frac{\partial\bar{u}_{k,1}}{\partial z_{k,1}}\dot{z}_{k,1} + \frac{\partial\bar{u}_{k,1}}{\partial g_{k,1}^{+}}\dot{g}_{k,1}^{+} + \frac{\partial\bar{u}_{k,1}}{\partial g_{k,1}^{-}}\dot{g}_{k,1}^{-} \\ &+ \frac{\partial\bar{u}_{k,1}}{\partial\varphi_k^{+}}\dot{\varphi}_k^{+} + \frac{\partial\bar{u}_{k,1}}{\partial\varphi_k^{-}}\dot{\varphi}_k^{-} + \frac{\partial\bar{u}_{k,1}}{\partial\dot{\varphi}_k^{+}}\ddot{\varphi}_k^{+} + \frac{\partial\bar{u}_{k,1}}{\partial\dot{\varphi}_k^{-}}\ddot{\varphi}_k^{-} \end{aligned} \tag{21}$$

Considering the continuous property [39], [40], there exists a constant $M_u > 0$ such that $(\dot{\bar{u}}_{k,1}(\boldsymbol{Y}, \boldsymbol{Z}, \boldsymbol{G}))^2 \le M_u, \forall(\boldsymbol{Y}, \boldsymbol{Z}, \boldsymbol{G}) \in Q_4$.

Therefore, within the compact set Q_4, we rewrite (A.18) as:

$$\begin{aligned} \dot{V}_{k,2} \le &-\sum_{j=1}^{2}\delta_{k,\min}z_{k,j}^2 - \sum_{j=1}^{2}\sigma_{k,\min}\left|z_{k,j}\right|^{\gamma+1} - \vartheta\phi_{k,2}^2 \\ &-\mu\left|\phi_{k,2}\right|^{\gamma+1} + \frac{1-\gamma}{2\varepsilon_{k,2}} + \frac{M_f + M_u}{2} \end{aligned} \tag{22}$$

Define a positive constant $\psi = (1-\gamma)/(2\varepsilon_{k,2}) + (M_f + M_u)/2$. Based on *Lemma 3*, we can rewrite (22) as follows:

$$\begin{aligned} \dot{V}_{k,2} &\le -k_1\left(\frac{1}{2}\left(z_{k,1}^2 + z_{k,2}^2 + \phi_{k,2}^2\right)\right) + \psi \\ &\quad -k_2\left(\frac{1}{2}\left(\left|z_{k,1}\right|^2 + \left|z_{k,2}\right|^2 + \left|\phi_{k,2}\right|^2\right)\right)^{(\gamma+1)/2} \\ &= -k_1V_{k,2} - k_2V_{k,2}^{(\gamma+1)/2} + \psi \end{aligned} \tag{23}$$

where k_1 and k_2 are two positive scalars that are defined as:

$$k_1 = \min\{2\delta_{k,\min}, 2\vartheta\},\ k_2 = \min\{2^{(\gamma+1)/2}\sigma_{k,\min}, 2^{(\gamma+1)/2}\mu\} \tag{24}$$

To facilitate the proof, we introduce a useful lemma:

Lemma 4 [42-44]: Considering the system $\dot{\boldsymbol{x}} = \boldsymbol{f}(\boldsymbol{x})$, suppose there exists a positive definite function $V(\boldsymbol{x})$ satisfying:

$$\dot{V}(\boldsymbol{x}) + k_1V(\boldsymbol{x}) + k_2V^q(\boldsymbol{x}) \le \Delta \tag{25}$$

where $\Delta > 0$, $k_1 > 0$, $k_2 > 0$, and $0 < q < 1$, then the system is practical finite-time stable, and its states can converge into a bounded region given by $\Omega = \{\boldsymbol{x} \mid V^q(\boldsymbol{x}) \le \Delta / (k_2(1-k_3))\}$, where $0 < k_3 < 1$. Besides, the settling time can be calculated by:

$$T \le \frac{1}{k_1(1-q)} \ln \frac{k_1 V^{1-q}(T_0) + k_2 k_3}{k_2 k_3} + T_0 \tag{26}$$

For better clarity, we can rewrite (23) as follows:

$$\dot{V}_{k,2} \le -k_1 V_{k,2} - k_2 k_3 V_{k,2}^{(\gamma+1)/2} - k_2(1-k_3) V_{k,2}^{(\gamma+1)/2} + \psi \tag{27}$$

where k_3 is a positive constant with a range of $0 < k_3 < 1$.

Choosing the parameters $\varepsilon_{k,2}$ and γ based on (28):

$$\frac{1-\gamma}{2\varepsilon_{k,2}} + \frac{M_f + M_u}{2} = \alpha_0 k_2 (1-k_3) \tag{28}$$

where the positive constant $\alpha_0 < (M_Z)^{(\gamma+1)/2}$.

Therefore, on $V_{k,2}(z_{k,1}, z_{k,2}, \phi_{k,2}) = M_Z$, we have $\dot{V}_{k,2} \le 0$. If $\boldsymbol{G}(t) \in Q_3, \forall t \ge 0$, we have: If $V_{k,2}(0) \le M_Z$, then $V_{k,2}(t) \le M_Z$ for all $t > 0$, and the expression in (17) is nonsingular. According to [39], there exist $\delta_{k,i}$, λ_i^+, λ_i^- with i = 1, 2, and u_c to achieve the inequality $|u_k - v_k| \le u_c$ for all $(\boldsymbol{Y}, \boldsymbol{Z}, \boldsymbol{G}) \in Q_4$. Thus, Q_3 is also an invariant set based on the analysis of the boundness of $g_{k,1}^-$ and $g_{k,1}^+$ in Part A. Under the initial conditions $\|\boldsymbol{Z}(0)\|^2 \le 2M_Z$ and $g_{k,i}^+(0) = g_{k,i}^-(0) = 0$ with i = 1, 2, we have $\boldsymbol{Z}(t) \in Q_2$ and $\boldsymbol{G}(t) \in Q_3$ for all $t > 0$. Finally, we conclude that the signals $z_{k,1}$, $z_{k,2}$, and $\phi_{k,2}$ of the closed-loop system are uniformly bounded.

Moreover, we can use the following two sets as examples.

$$\begin{cases} \Omega_{\text{in}} = \left\{ z_{k,1}, z_{k,2}, \phi_{k,2} \middle| V_{k,2}^{(\gamma+1)/2} \le \dfrac{\psi}{k_2(1-k_3)} \right\} \\ \Omega_{\text{out}} = \left\{ z_{k,1}, z_{k,2}, \phi_{k,2} \middle| V_{k,2}^{(\gamma+1)/2} > \dfrac{\psi}{k_2(1-k_3)} \right\} \end{cases} \tag{29}$$

Case 1: If $z_{k,1}, z_{k,2}, \phi_{k,2} \in \Omega_{\text{out}}$, then $-k_2(1-k_3) V_{k,2}^{(\gamma+1)/2} + \psi < 0$. Therefore, we can rewrite (27) as:

$$\dot{V}_{k,2} \le -k_1 V_{k,2} - k_2 k_3 V_{k,2}^{(\gamma+1)/2} \tag{30}$$

Integrating both sides of (30) yields:

$$\int_{V_{k,2}(t_0)}^{V_{k,2}(t_s)} \frac{V_{k,2}^{-(\gamma+1)/2}}{k_1 V_{k,2}^{(1-\gamma)/2} + k_2 k_3} dV_{k,2} \le \int_{t_0}^{t_s} (-1)\, dt \tag{31}$$

Then, we obtain the settling time t_s:

$$t_s \le \frac{2}{k_1(1-\gamma)} \ln \left(\frac{k_2 k_3 + k_1 V_{k,2}^{(1-\gamma)/2}(t_0)}{k_2 k_3} \right) + t_0 \tag{32}$$

Case 2: If $z_{k,1}, z_{k,2}, \phi_{k,2} \in \Omega_{\text{in}}$, based on Case 1, they remain within Ω_{in}. Actually, the above proof reproduces the *Lemma 4*.

From the definition of $\bar{u}_{k,1}$ and u_k in (19), it follows that both of them are continuous functions. Within the set Q_4, we have $|\bar{u}_{k,1}| \le \Phi_k(z_{k,1}, g_{k,1}^-, g_{k,1}^+, x_{dk}, \dot{x}_{dk}, \varphi_k^+, \dot{\varphi}_k^+, \varphi_k^-, \dot{\varphi}_k^-)$ and $|u_k| \le \Theta_k(z_{k,1}, z_{k,2}, \phi_{k,2}, g_{k,1}^-, g_{k,2}^-, g_{k,1}^+, g_{k,2}^+, x_{dk}, \dot{x}_{dk}, \varphi_k^+, \dot{\varphi}_k^+, \varphi_k^-, \dot{\varphi}_k^-)$. Φ_k and Θ_k are continuous functions. φ_k^+ and φ_k^- are shown in (13). Considering the continuous property [39], [40], both Φ_k and Θ_k have a maximum within the compact set Q_4. Therefore, both $\bar{u}_{k,1}$ and u_k are bounded under the initial conditions $\|\boldsymbol{Z}(0)\|^2 \le 2M_Z$ and $g_{k,i}^+(0) = g_{k,i}^-(0) = 0$, where i = 1, 2.

Remark 3: $\beta_{k,Amp}$, $\beta_{k,bias}$, and ξ affect the shape of envelopes. Increasing $\beta_{k,Amp}$ and $\beta_{k,bias}$ while decreasing ξ helps enhance the controller's tolerance to tracking errors. Conversely, decreasing $\beta_{k,Amp}$ and $\beta_{k,bias}$ while increasing ξ reduces the error tolerance of the controller. λ_1^+, λ_1^-, λ_2^+, and λ_2^- affect the convergence speed of the envelopes. Increasing them will speed up the convergence of envelopes. However, if they are too large, they will cause unsmooth velocity. Their values should be assigned in ascending order. If unsmooth velocity occurs, the values should be reduced. To ensure the stability of the system, the value of γ should be in the range of $0 < \gamma \le 1$. Within this range, a larger value should be selected to avoid discontinuous fluctuations in the control input. In contrast to the effect of γ, excessively large values of $\delta_{k,1}$, $\delta_{k,2}$, $\sigma_{k,1}$, and $\sigma_{k,2}$ will cause fluctuations in control inputs. The values of $\delta_{k,1}$, $\delta_{k,2}$, $\sigma_{k,1}$, and $\sigma_{k,2}$ should be assigned in ascending order. If fluctuations occur in the control input, their values should be reduced. $\varepsilon_{k,2}$ is the time constant of the filter. Three values of $\varepsilon_{k,2}$ are selected to show their influence on the trajectory and control input (see Fig. A3 in the supplementary material). When $\varepsilon_{k,2}$ is set to a large value like 0.9, the control input exhibits fluctuations, causing slight fluctuations in the trajectory. When the value of $\varepsilon_{k,2}$ is reduced to 0.1, the fluctuations in the control input are significantly reduced but still present. When $\varepsilon_{k,2}$ is further reduced to 0.01, the fluctuation disappears. However, if $\varepsilon_{k,2}$ is too small, the filter allows some high-frequency noise to pass through, potentially introducing this noise into the control input. Therefore, to select an appropriate value for $\varepsilon_{k,2}$, it is advisable to gradually reduce it from a large value (less than 1) until the fluctuations in the control input disappear. Figs. A1-A3 (in the supplementary material) illustrate the influence of these parameters on trajectory envelopes and control inputs.

IV. Simulation and Experiment

A. Results of the proposed control scheme

Fig. 3 depicts the block diagram of the control scheme in the experiments. The motor driver operates in velocity mode. The distribution of cable forces can be finished based on Newton's second law. The force tracker utilizes PI control to achieve force tracking. Fig. 4 illustrates the experimental setup, which includes a laser tracker to record the position of the moving platform and uses force sensors for force feedback.

For the CDR with one cable, the mass of the load m_r = 0.51 kg. The inherent envelope is $\varphi_k^- = \varphi_k^+ = \beta_{k,Amp} e^{-\xi t} + \beta_{k,bias}$ m with $\beta_{1,Amp}$ = 0.32, $\beta_{1,bias}$ = 0.04, and ξ = 1. The dimensionless coefficients for the variable envelopes are $\lambda_1^+ = 2$, $\lambda_1^- = 2$, $\lambda_2^+ = 2$, and $\lambda_2^- = 2$. The dimensionless control parameters are chosen as $\gamma = 0.75, \delta_{1,1} = 10, \sigma_{1,1} = 1, \delta_{1,2} = 3, \sigma_{1,2} = 1$, and $\varepsilon_{1,2} = 0.01$.

Fig. 5 illustrates the trajectory tracking effect and cable forces, while Fig. 6 displays the torque index of the motor, with an index of 1 representing one hundred of the motor's rated torque (1.01 Nm). The motor driver provides a hard limit on the output torque. We reduce the upper limit of the output torque index to 12 (Limit 1) and 10 (Limit 2), respectively. In simulation, we set the limits for the control input u_k as follows: Limit 1: $u_{\max,1}$ = 5.2 N; Limit 2: $u_{\max,1}$ = 5.03 N. Without any limits, the maximum tracking error in simulation is 3×10^{-4} m,

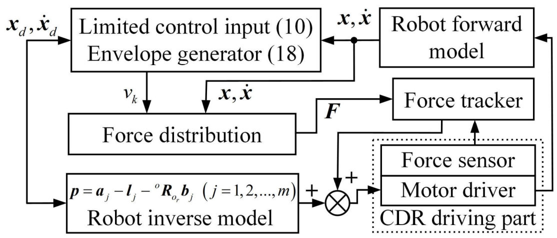

Fig. 3. Block diagram of the designed controller.

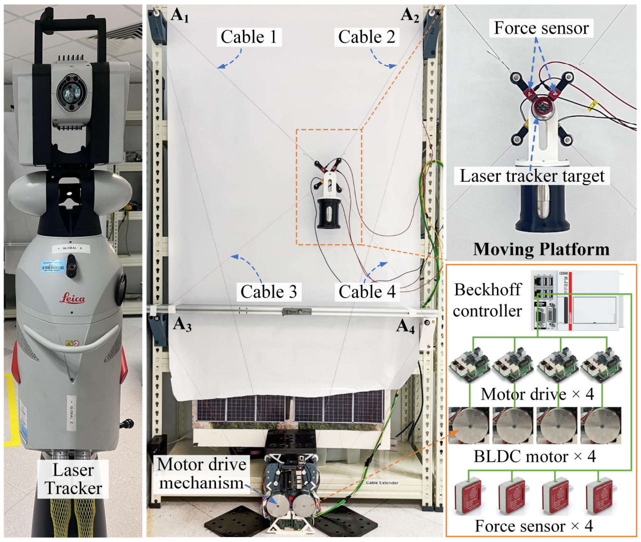

Fig. 4. Experimental setup.

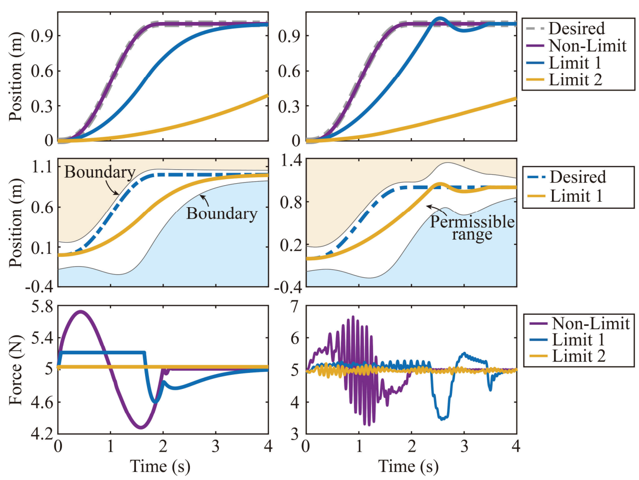

Fig. 5. Trajectory, trajectory envelope, and cable forces of the one-cable CDR. (a) Simulation result. (b) Experimental result.

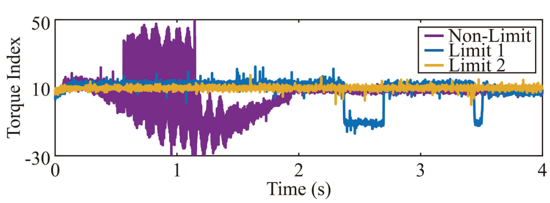

Fig. 6. Motor output torque index.

and the maximum cable force is 5.7 N. Experimental results show a maximum tracking error of 4.3×10^{-3} m and a maximum cable force of 6.7 N. Despite some differences between the simulations and experiments, both consistently demonstrated similar trends in trajectory and cable force.

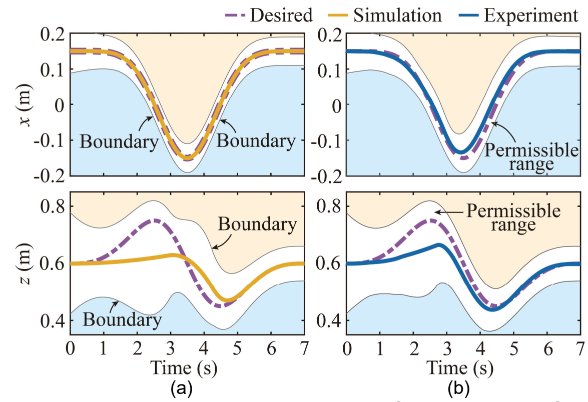

Fig. 7. Trajectory and trajectory envelope of the two-cable CDR. (a) Simulation result. (b) Experimental result.

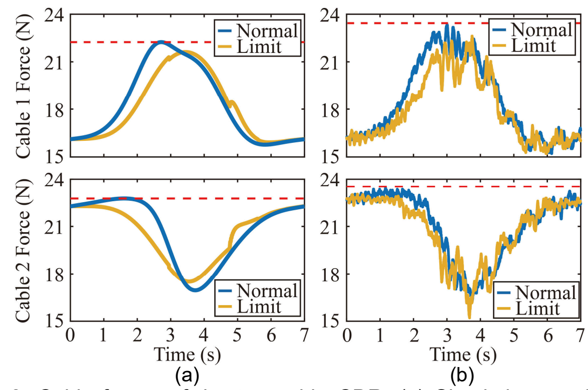

Fig. 8. Cable forces of the two-cable CDR. (a) Simulation result. (b) Experimental result.

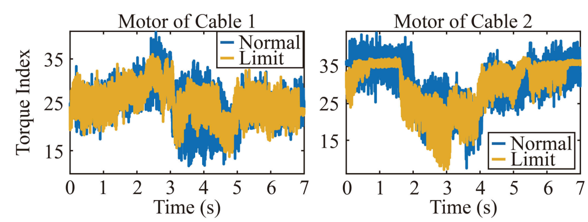

Fig. 9. Motor output torque index.

In Fig. 6, there is a clear difference between the motor torque index without output limits and the motor torque index with output limits. When the output torque of the motor reaches its upper limit, the actual trajectory significantly deviates from the target trajectory. As the constraint on motor output torque increases, the trajectory tracking error also grows. In the scenario labeled "Limit 2", although the actual trajectory tracking error has reached 0.89 m, the controller still maintains trajectory tracking without any loss of control. This further validates the stability of the tracking controller even when subjected to constrained control inputs. The capability to maintain stable tracking despite significant deviations from the target trajectory can be attributed to the adjustable trajectory envelope. As shown in Fig. 5, when the actual trajectory deviates from the target trajectory due to the limited output torque, the trajectory envelope is actively adjusted and expanded to ensure the actual trajectory remains within the allowable range. The controller's objective shifts from accurately tracking target trajectories to maintaining the actual trajectory within the specified range, thus ensuring controllable tracking even when control inputs reach their upper limits.

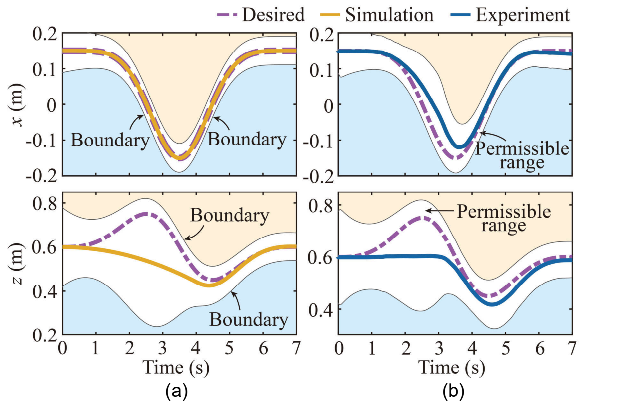

Fig. 10. Trajectory and trajectory envelope of the four-cable CDR. (a) Simulation result. (b) Experimental result.

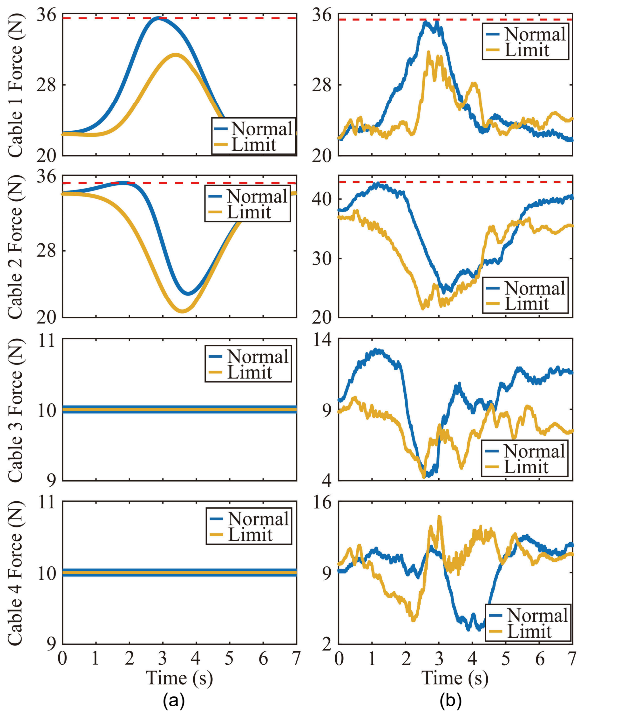

Fig. 11. Cable forces of the four-cable CDR. (a) Simulation result. (b) Experimental result.

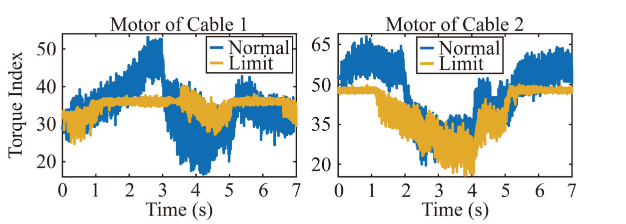

Fig. 12. Motor output torque index.

For the CDR with two and four cables, the mass of the load m_r = 3 kg. The inherent envelopes are expressed as $\varphi_k^- = \varphi_k^+ = \beta_{k,Amp}e^{-\xi t} + \beta_{k,bias}$ m with $\beta_{1,Amp}$ = 0.32, $\beta_{1,bias}$ = 0.04, $\beta_{2,Amp}$ = 0.32, $\beta_{2,bias}$ = 0.06, and ξ = 1. The dimensionless coefficients for the variable envelopes are $\lambda_1^+ = 20$, $\lambda_1^- = 20$, $\lambda_2^+ = 2$, and λ_2^- = 2. The dimensionless control parameters are chosen as γ = 0.75, $\delta_{1,1}$= 500, $\sigma_{1,1}$ = 1, $\delta_{1,2}$= 3, $\sigma_{1,2}$ = 1, $\delta_{2,1}$= 500, $\sigma_{2,1}$ = 1, $\delta_{2,2}$ = 3, $\sigma_{2,2}$ = 1, $\varepsilon_{1,2}$ = 0.01, and $\varepsilon_{2,2}$ = 0.01.

The coordinates of the four anchor points shown in Fig. 4 are: A_1 (-0.5435, 1.2199) m, A_2 (0.5435, 1.2199) m, A_3 (-0.5554, 0) m, and A_4 (0.5554, 0) m. In the simulation, for the two-cable CDR, we set the limit for u_2 as follows: $u_{\max,2}$ = 29.42 N, $u_{\min,2}$ = 28.9 N. For the four-cable CDR, we set the limit for u_2 as follows: $u_{\max,2}$ = 29.34 N, $u_{\min,2}$ = 28.34 N. In the experiment, the upper limit of the output torque index for two motors of the two-cable CDR was set to 36. For the four-cable CDR, the upper limit for the output torque index of the motor on A_1 side was set at 36, while for the A_2 side motor, it was set at 48.

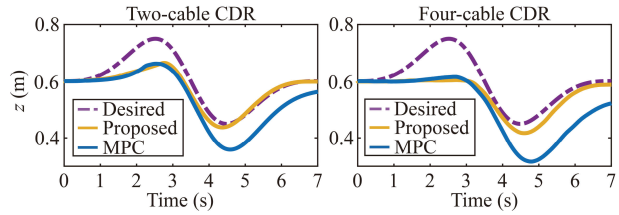

Fig. 13. Trajectories of the proposed controller and MPC controller.

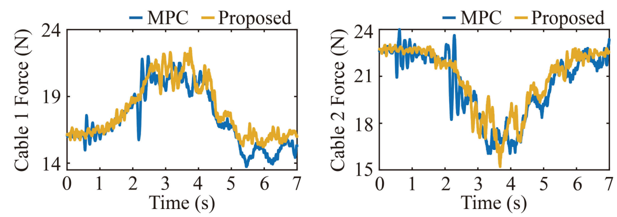

Fig. 14. Comparison of cable forces using the two-cable CDR.

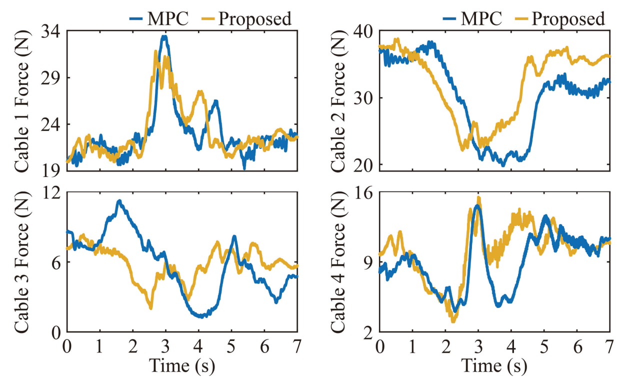

Fig. 15. Comparison of cable forces using the four-cable CDR.

Since u_1 is not limited in the simulation, the motion along the x-direction in Fig. 7 and Fig. 10 remains unaffected, while the trajectory along the z-direction has deviated. Due to the lack of ideal experimental conditions, the actual motion along the x and z directions cannot be perfectly separated. Therefore, not only does the experimental trajectory along the z-direction deviate from the target trajectory (maximum error: 0.097 m), but the trajectory along the x-direction also deviates from the target value (maximum error: 0.031 m). The phenomenon is similarly observed in the four-cable CDR. As shown in Fig. 10, the maximum error in the experimental trajectory along the x-direction is 0.073 m, while along the z-direction it reaches 0.145 m. Despite such significant deviations, the trajectory envelopes depicted in Figs. 7 and 10 both envelop the actual trajectories. When motor output torque is limited, Cable 1's tension in the two-cable CDR decreases from 23.4 N to 22.5 N, and Cable 2's tension is reduced from 23.4 to 22.9 N. Fig. 9 compares the motor torque index with and without output limits. To further illustrate the differences between scenarios with and without output limits, we conducted experiments on a four-cable CDR. Results show that tensions in Cable 1 decrease from 35.2 N to 31.8 N, and tensions in Cable 2 decrease from 42.7 N to 38.7 N, as depicted in Fig. 11. Fig. 12 more clearly shows the differences between the normal output torque and the constrained output torque. The results of experiments conducted on single, two, and four-cable CDRs show that the trajectory envelope generator is capable of actively adjusting and expanding the envelope lines when the control inputs reach their upper limits. This shifts the objective of the tracking controller from accurately tracking the target trajectory to maintaining the actual trajectory within a specified range. Thus, it prevents continuous increases in control inputs. The tracking controller ensures that the actual trajectory always remains within the permissible range, achieving stable trajectory tracking when control inputs reach their upper limits.

B. Comparison with MPC control scheme

Considering that model predictive control (MPC) could also handle constraint problems, we applied MPC to two-cable and four-cable CDRs to conduct experiments and compared its results with those of the proposed control scheme. The trajectories and cable forces are shown in Figs. 13 to 15.

Unlike the control scheme proposed in this paper, MPC does not have the concept of envelope lines. Figs. 13 and 15 reveal that when the motor torque reaches its upper limit, the actual trajectories under both control schemes deviate from the target trajectory, with greater deviation observed under MPC. Compared to MPC, the proposed control scheme allows the actual trajectory to converge more quickly towards the target trajectory. This occurs because MPC considers both trajectory tracking accuracy and control input as optimization objectives, leading to a compromise where tracking accuracy is sacrificed to ensure that the control input meets the constraints. This compromise becomes more pronounced when control inputs are limited. In contrast, the proposed control scheme prioritizes trajectory tracking accuracy above all. The control input is used by the trajectory envelope generator to actively adjust the envelope, ensuring that the actual trajectory remains as close as possible to the target trajectory within the available range of the control inputs.

V. Conclusion

In this paper, a specialized tracking controller was developed to address the trajectory tracking problem of CDRs under constrained control inputs. Integrated with a trajectory envelope generator, the controller ensures that the actual trajectory remains within a specified allowable range, even when control inputs reach their upper limits. The generator quantitatively links the limited control input to the permissible range of the actual trajectory and actively adjusts this range. When control inputs are limited, the objective of the controller shifts from accurately tracking target trajectories to maintaining the actual trajectory within the specified range, which prevents the continuous increase of control inputs and ensures the trajectory tracking remains controllable. Compared to model predictive control, the proposed controller enables the actual trajectory to converge faster to the target trajectory under constrained control inputs. Experiments were conducted on a CDR with configurations of one, two, and four cables. The results verified that the controller maintained stable tracking capabilities, even with a tracking error of up to 0.89 m. The controller effectively expanded the trajectory envelope to consistently encompass the actual trajectory, thereby ensuring controllable trajectory tracking without mid-course failures.

Appendix

A. The partial derivatives in (14) and (15)

$$\frac{\partial z_{k,1}}{\partial \varphi_k}=\frac{2\pi\left(\left(\tan\left(\dfrac{2\pi\varphi_k+\pi\left(\varphi_{g,k}^- - \varphi_{g,k}^+\right)}{2\left(\varphi_{g,k}^- + \varphi_{g,k}^+\right)}\right)\right)^2+1\right)}{2\left(\varphi_{g,k}^- + \varphi_{g,k}^+\right)} \tag{A.1}$$

$$\begin{aligned}\frac{\partial z_{k,1}}{\partial \varphi_{g,k}^-}&=\left(\left(\tan\left(\frac{2\pi\varphi_k+\pi\left(\varphi_{g,k}^- - \varphi_{g,k}^+\right)}{2\left(\varphi_{g,k}^- + \varphi_{g,k}^+\right)}\right)\right)^2+1\right)\\ &\times\left(\frac{\pi}{2\left(\varphi_{g,k}^- + \varphi_{g,k}^+\right)}-\frac{2\left(2\pi\varphi_k+\pi\left(\varphi_{g,k}^- - \varphi_{g,k}^+\right)\right)}{\left(2\left(\varphi_{g,k}^- + \varphi_{g,k}^+\right)\right)^2}\right)\end{aligned} \tag{A.2}$$

$$\begin{aligned}\frac{\partial z_{k,1}}{\partial \varphi_{g,k}^+}&=-\left(\left(\tan\left(\frac{2\pi\varphi_k+\pi\left(\varphi_{g,k}^- - \varphi_{g,k}^+\right)}{2\left(\varphi_{g,k}^- + \varphi_{g,k}^+\right)}\right)\right)^2+1\right)\\ &\times\left(\frac{\pi}{2\left(\varphi_{g,k}^- + \varphi_{g,k}^+\right)}+\frac{2\left(2\pi\varphi_k+\pi\left(\varphi_{g,k}^- - \varphi_{g,k}^+\right)\right)}{\left(2\left(\varphi_{g,k}^- + \varphi_{g,k}^+\right)\right)^2}\right)\end{aligned} \tag{A.3}$$

Substituting (17) into (A.2) yields:

$$\frac{\partial z_{k,1}}{\partial \varphi_{g,k}^-}=\left((z_{k,1})^2+1\right)\left(\frac{4\pi\left(\varphi_{g,k}^+ - \varphi_k\right)}{\left(2(\varphi_{g,k}^- + \varphi_{g,k}^+)\right)^2}\right) \tag{A.4}$$

By combining (18) and (A.4), we have $\partial z_{k,1}/\partial\varphi_{g,k}^- > 0$. Likewise, we obtain $\partial z_{k,1}/\partial\varphi_{g,k}^+ < 0$. The role of the positive or negative values of the two variables should be considered in the context of (14) and (15). In (14), since there is a positive sign in front of $\partial z_{k,1}/\partial\varphi_{g,k}^-$, the term formed by $+(\partial z_{k,1}/\partial\varphi_{g,k}^-)^{-1}$ results in an overall positive value. In (15), there is a negative sign in front of $\partial z_{k,1}/\partial\varphi_{g,k}^+$, hence the term formed by $-(\partial z_{k,1}/\partial\varphi_{g,k}^+)^{-1}$ still results in an overall positive value.

B. Derivation for Theorem 1

Select the Lyapunov candidate $V_{k,1}=(1/2)z_{k,1}^2$. By combining (13)-(17), the derivative of $V_{k,1}$ is obtained:

$$\begin{aligned}\dot V_{k,1}&=z_{k,1}\left(\partial_k^{z\varphi}\left(x_{k,2}-\dot x_{dk}+g_{k,2}^- - g_{k,2}^+\right)+\partial_k^{z\varphi^+}\dot\varphi_k^+\right.\\ &\left.+\partial_k^{z\varphi^-}\dot\varphi_k^- + \partial_k^{z\varphi}\left(\lambda_1^+ g_{k,1}^+ - \lambda_1^- g_{k,1}^-\right)\right)\end{aligned} \tag{A.5}$$

To eliminate $x_{k,2}$, $g_{k,2}^-$ and $g_{k,2}^+$ in (A.5), let's introduce an intermediate variable $z_{k,2}$ and the virtual control input $\overline{u}_{k,1}$:

$$z_{k,2}=x_{k,2}+g_{k,2}^- - g_{k,2}^+ - \overline{u}_{k,1} \tag{A.6}$$

$$\begin{aligned}\overline{u}_{k,1}&=\dot x_{dk}-\left(\partial_k^{z\varphi}\right)^{-1}\left(\partial_k^{z\varphi^+}\dot\varphi_k^+ + \partial_k^{z\varphi^-}\dot\varphi_k^-\right)-\left(\lambda_1^+ g_{k,1}^+ - \lambda_1^- g_{k,1}^-\right)\\ &-\left(\partial_k^{z\varphi}\right)^{-1}\left(\delta_{k,1}z_{k,1}+\sigma_{k,1}sign(z_{k,1})\left|z_{k,1}\right|^{\gamma}\right)\end{aligned} \tag{A.7}$$

where $\delta_{k,1}, \sigma_{k,1} > 0$ and $1 > \gamma > 0$.

To avoid solving the derivative of $\bar{u}_{k,1}$ when deriving the control input u_k later, we introduce the following first-order filter [38]:

$$\varepsilon_{k,2}\dot{\omega}_{k,2} + \omega_{k,2} = \bar{u}_{k,1},\ \varepsilon_{k,2} > 0 \tag{A.8}$$

Defining $\phi_{k,2}$ as the error between $\bar{u}_{k,1}$ and $\omega_{k,2}$, we have:

$$\dot{\omega}_{k,2} = \left(\bar{u}_{k,1} - \omega_{k,2}\right)/\varepsilon_{k,2} = -\phi_{k,2}/\varepsilon_{k,2} \tag{A.9}$$

Then, the expression of $z_{k,2}$ in (A.6) can be rewritten as:

$$z_{k,2} = x_{k,2} + g_{k,2}^{-} - g_{k,2}^{+} - \omega_{k,2} \tag{A.10}$$

By substituting the virtual control input $\bar{u}_{k,1}$ (A.7) and (A.9) in (A.5), we obtain:

$$\dot{V}_{k,1} = z_{k,1}\partial_k^{z\varphi} z_{k,2} + z_{k,1}\partial_k^{z\varphi}\phi_{k,2} - \delta_{k,1}z_{k,1}^2 - \sigma_{k,1}\left|z_{k,1}\right|^{\gamma+1} \tag{A.11}$$

Next, we select the Lyapunov candidate as follows:

$$V_{k,2} = (1/2)\left(z_{k,1}^2 + z_{k,2}^2 + \phi_{k,2}^2\right) \tag{A.12}$$

Combining (9), (13)-(17), (A.8), (A.10) with (A.12), we obtain:

$$\begin{aligned}\dot{V}_{k,2} = \dot{V}_{k,1} + z_{k,2}\left(u_k + f_{k,2}(\boldsymbol{x}) - \lambda_2^{-} g_{k,2}^{-} + \lambda_2^{+} g_{k,2}^{+} - \dot{\omega}_{k,2}\right) \\ + \phi_{k,2}\left(\dot{\omega}_{k,2} - \dot{\bar{u}}_{k,1}\right)\end{aligned} \tag{A.13}$$

Substituting (19) into (A.13) yields:

$$\begin{aligned}\dot{V}_{k,2} \le -\sum_{j=1}^{2}\left(\delta_{k,j} - \frac{1}{2}\right)z_{k,j}^2 - \sum_{j=1}^{2}\sigma_{k,j}\left|z_{k,j}\right|^{\gamma+1} \\ -\left(\frac{1}{\varepsilon_{k,2}} - \frac{1}{2} - \frac{1}{2}\left(\partial_k^{z\varphi}\right)^2\right)\phi_{k,2}^2 + \frac{1}{2}f_{k,2}^2(\boldsymbol{x}) + \frac{1}{2}\dot{\bar{u}}_{k,1}^2\end{aligned} \tag{A.14}$$

To facilitate the proof, let's introduce two lemmas and two positive constants $\delta_{k,\min}$ and $\sigma_{k,\min}$:

$$\delta_{k,\min} = \min\{\delta_{k,1} - 1/2, \delta_{k,2} - 1/2\},\ \sigma_{k,\min} = \min\{\sigma_{k,1}, \sigma_{k,2}\} \tag{A.15}$$

Lemma 2 [44]: There exist $a \ge 0$ and $1 > \gamma > 0$ such that:

$$a^{\gamma+1} \le (1+\gamma)a^2/2 + (1-\gamma)/2 \tag{A.16}$$

Lemma 3 [44]: There exist a, $b \ge 0$ and $1 \ge \gamma > 0$ such that:

$$(a+b)^{\gamma} \le a^{\gamma} + b^{\gamma} \tag{A.17}$$

Based on (A.14) and *Lemma 2*, we obtain:

$$\begin{aligned}\dot{V}_{k,2} \le -\sum_{j=1}^{2}\delta_{k,\min}z_{k,j}^2 - \sum_{j=1}^{2}\sigma_{k,\min}\left|z_{k,j}\right|^{\gamma+1} - \vartheta\phi_{k,2}^2 \\ -\mu\left|\phi_{k,2}\right|^{\gamma+1} + \frac{1-\gamma}{2\varepsilon_{k,2}} + \frac{f_{k,2}^2(\boldsymbol{x})}{2} + \frac{\dot{\bar{u}}_{k,1}^2}{2}\end{aligned} \tag{A.18}$$

where

$$\begin{cases}\mu = 1/\varepsilon_{k,2} - 1/2 - (1/2)(\partial_k^{z\varphi})^2 \\ \vartheta = (1-\gamma)(1/\varepsilon_{k,2} - 1/2 - (1/2)(\partial_k^{z\varphi})^2)/2\end{cases} \tag{A.19}$$

References

[1] J. P. Merlet, "MARIONET, a family of modular wire-driven parallel robots" in *Advances in Robot Kinematics: Motion in Man and Machine*, Netherlands: Springer, 2010, pp. 53–61.

[2] H. Jamshidifar, M. Rushton, and A. Khajepour, "A reaction-based stabilizer for nonmodel-based vibration control of cable-driven parallel robots," *IEEE Trans. Robot.*, vol. 37, no. 2, pp. 667–674, 2020.

[3] R. de Rijk, M. Rushton, and A. Khajepour, "Out-of-plane vibration control of a planar cable-driven parallel robot," *IEEE/ASME Trans. Mechatron.*, vol. 23, no. 4, pp. 1684–1692, 2018.

[4] H. Sun, X. Tang, Z. Cui, *et al.*, "Dynamic response of spatial flexible structures subjected to controllable force based on cable-driven parallel robots," *IEEE/ASME Trans. Mechatron.*, vol. 25, no. 6, pp. 2801–2811, 2020.

[5] R. Ramadour, F. Chaumette, and J. P. Merlet, "Grasping objects with a cable-driven parallel robot designed for transfer operation by visual servoing," in *IEEE International Conference on Robotics and Automation* (ICRA), pp. 4463–4468, 2014.

[6] A. Pott, H. Mütherich, W. Kraus, *et al.*, "Cable-driven parallel robots for industrial applications: The IPAnema system family," in *Proc. IEEE ISR*, pp. 1–6, 2013.

[7] Z. Shao, G. Xie, Z. Zhang, et al, "Design and analysis of the cable-driven parallel robot for cleaning exterior wall of buildings," *Int. J. Adv. Robot. Syst.*, vol. 18, no. 1, 1729881421990313, 2021.

[8] J. Wang, C. Hu, G. Ning, *et al.*, "A novel miniature spring-based continuum manipulator for minimally invasive surgery: Design and evaluation," *IEEE/ASME Trans. Mechatron.*, vol. 28, no. 5, pp. 2716–2727, 2023.

[9] A. Zargari, Z. A. Castrejon, D. Kim, *et al.*, "Cable-Driven Parallel Robot for Warehouse Monitoring Tasks" in *IEEE 13th Annual Computing and Communication Workshop and Conference*, pp. 1085–1090, 2023.

[10] C. Sancak and M. Itik, "Out-of-plane vibration suppression and position control of a planar cable-driven robot," *IEEE/ASME Trans. Mechatron.*, vol. 27, no. 3, pp. 1311–1320, 2022

[11] C. Sancak, M. Itik, and T. T. Nguyen, "Position control of a fully constrained planar cable-driven parallel robot with unknown or partially known dynamics," *IEEE/ASME Trans. Mechatron.*, vol. 28, no. 3, pp. 1605–1615, 2023.

[12] J. Begey, L. Cuvillon, M. Lesellier, *et al.*, "Dynamic control of parallel robots driven by flexible cables and actuated by position-controlled winches," *IEEE Trans. Robot.*, vol. 35, no. 1, pp. 286–293, 2018.

[13] Z. Zake, F. Chaumette, N. Pedemonte, *et al.*, "Vision-based control and stability analysis of a cable-driven parallel robot," *IEEE Robot. Autom. Lett.*, vol. 4, no. 2, pp. 1029–1036, 2019.

[14] M. T. Vu, K. H. Hsia, F. F. M. El-Sousy, *et al.*, "Adaptive fuzzy control of a cable-driven parallel robot," *Math.*, vol. 10, no. 20, pp. 3826, 2022.

[15] B. Zhang, W. Shang, S. Cong, *et al.*, "Dual-loop dynamic control of cable-driven parallel robots without online tension distribution," *IEEE Trans. Syst. Man Cybern. Syst.*, vol. 52, no. 10, pp. 6555–6568, 2022.

[16] H. Ji, W. Shang, and S. Cong, "Adaptive synchronization control of cable-driven parallel robots with uncertain kinematics and dynamics," *IEEE Trans. Ind. Electron.*, vol. 68, no. 9, pp. 8444–8454, 2020.

[17] F. Xie, W. Shang, B. Zhang, *et al.*, "High-precision trajectory tracking control of cable-driven parallel robots using robust synchronization," *IEEE Trans. Ind. Inform.*, vol. 17, no. 4, pp. 2488–2499, 2020.

[18] C. Gosselin, and S. Foucault, "Dynamic point-to-point trajectory planning of a two-DOF cable-suspended parallel robot," *IEEE Trans. Robot.*, vol. 30, no. 3, pp. 728–736, 2014.

[19] L. Tang, X. Tang, X. Jiang, *et al.*, "Dynamic trajectory planning study of planar two-dof redundantly actuated cable-suspended parallel robots," *Mechatron.*, vol. 30, pp. 187–197, 2015.

[20] Y. Shi, J. Wang, S. Li, *et al.*, "Tracking control of cable-driven planar robot based on discrete-time recurrent neural network with immediate discretization method," *IEEE Trans. Ind. Inform.*, vol. 19, no. 6, pp. 7414–7423, 2022.

[21] Y. Lu, C. Wu, W. Yao, *et al.*, "Deep reinforcement learning control of fully-constrained cable-driven parallel robots," *IEEE Trans. Ind. Electron.*, vol. 70, no. 7, pp. 7194–7204, 2022.

[22] W. Shang, B. Zhang, F. Zhang, and S. Cong, "Synchronization control in the cable space for cable-driven parallel robots," *IEEE Trans. Ind. Electron.*, vol. 66, no. 6, pp. 4544–4554, 2019.

[23] E. Idà, T. Bruckmann, and M. Carricato, "Rest-to-rest trajectory planning for underactuated cable-driven parallel robots," *IEEE Trans. Robot.*, vol. 35, no. 6, pp. 1338–1351, 2019.

[24] E. Idá, A. Berti, T. Bruckmann, *et al.*, "Rest-to-rest trajectory planning for planar underactuated cable-driven parallel robots," in *Cable-Driven Parallel Robots: Proceedings of the Third International Conference on Cable-Driven Parallel Robots*, C. Gosselin, P.Cardou, T. Bruckmann, and A. Pott (Eds.) Switzerland : Springer, 2018, pp. 207–218.

[25] C. Song and D. Lau, "Workspace-based model predictive control for cable-driven robots," *IEEE Trans. Robot.*, vol. 38, no. 4, pp. 2577–2596, 2022.

[26] J. C. Santos, M. Gouttefarde, and A. Chemori, "A nonlinear model predictive control for the position tracking of cable-driven parallel robots," *IEEE Trans. Robot.*, vol. 38, no. 4, pp. 2597–2616, 2022.

[27] H. Jabbari Asl and J. Yoon, "Robust trajectory tracking control of

cable-driven parallel robots," *Nonlinear Dyn.*, vol. 89, pp. 2769–2784, 2017.

[28] A. Ameri, A. Molaei, M. A. Khosravi, *et al.*, "Control-based tension distribution scheme for fully constrained cable-driven robots," *IEEE Trans. Ind. Electron.*, vol. 69, no. 11, pp. 11383–11393, 2022.

[29] H. J. Asl and F. Janabi-Sharifi, "Adaptive neural network control of cable-driven parallel robots with input saturation," *Eng. Appl. Artif. Intell.*, vol. 65, pp. 252–260, 2017.

[30] M. R. J. Harandi, S. A. Khalilpour, and H. D. Taghirad, "Adaptive energy shaping control of a 3-DOF underactuated cable-driven parallel robot," *IEEE Trans. Ind. Inform.*, vol. 19, no. 6, pp. 7552–7560, 2022.

[31] Z. Chen, X. Wang, and Y. Cheng, "Adaptive finite-time disturbance observer-based recursive fractional-order sliding mode control of redundantly actuated cable driving parallel robots under disturbances and input saturation," *J. Vib. Control.*, vol. 29 no. 3–4, pp. 675–688, 2023.

[32] X. Liang, S. S. Ge, and B. V. E. How, "Constrained control for a class of vessel operations: Positioning under environmental and shielding effects," *Eur. J. Control.*, vol. 69, pp. 100760, 2023.

[33] Y. Zhang, X. Liang, D. Li, S. S. Ge, *et al.*, "Adaptive safe reinforcement learning with full-state constraints and constrained adaptation for autonomous vehicles," *IEEE T. Cybern.*, vol. 54, no. 3, pp. 1907-1920, 2023.

[34] K. Yong, M. Chen, Y. Shi, and Q. Wu, "Flexible performance-based robust control for a class of nonlinear systems with input saturation," *Automatica*, vol. 122, pp. 109268, 2020.

[35] R. Ji, B. Yang, J. Ma, and S. S. Ge, "Saturation-tolerant prescribed control for a class of MIMO nonlinear systems," *IEEE T. Cybern.*, vol. 52, no.12, pp. 13012-13026, 2021.

[36] J. Bettega, D. Richiedei, and A. Trevisani, "Using pose-dependent model predictive control for path tracking with bounded tensions in a 3-DOF spatial cable suspended parallel robot," *Machines*, vol. 10, no. 6, pp. 453, 2022.

[37] L. Farina and S. Rinaldi, Positive Linear Systems: Theory and Applications. John Wiley & Sons, 2011.

[38] D. Swaroop, J. K. Hedrick, P. P. Yip, and J. C. Gerdes, "Dynamic surface control for a class of nonlinear systems," *IEEE Trans. Autom. Control.*, vol. 45, no. 10, pp. 1893-1899, 2000.

[39] M. Chen, G. Tao, and B. Jiang, "Dynamic surface control using neural networks for a class of uncertain nonlinear systems with input saturation," *IEEE Trans. Neural Netw. Learn. Syst.*, vol. 26, no. 9, pp. 2086-2097, 2014.

[40] D. Wang and J. Huang, "Neural network-based adaptive dynamic surface control for a class of uncertain nonlinear systems in strict-feedback form," *IEEE Trans. Neural Netw.*, vol. 16, no. 1, pp. 195-202, 2005.

[41] C. Wen, J. Zhou, Z. Liu, and H. Su, "Robust adaptive control of uncertain nonlinear systems in the presence of input saturation and external disturbance," *IEEE Trans. Autom. Control.*, vol. 56, no. 7, pp. 1672-1678, 2011.

[42] Q. Yao, "Adaptive finite-time sliding mode control design for finite-time fault-tolerant trajectory tracking of marine vehicles with input saturation," *J. Frankl. Inst.-Eng. Appl. Math.*, vol. 357, no. 18, pp. 13593-13619, 2020.

[43] S. Yu, X. Yu, B. Shirinzadeh, and Z. Man, "Continuous finite-time control for robotic manipulators with terminal sliding mode," *Automatica*, vol. 41, no. 11, pp. 1957-1964, 2005.

[44] K. Liu, R. Wang, X. Wang, *et al.*, "Anti-saturation adaptive finite-time neural network based fault-tolerant tracking control for a quadrotor UAV with external disturbances," *Aerosp. Sci. Technol.*, vol. 115, pp. 106790, 2021.

[45] C. Qian and W. Lin, "Non-Lipschitz continuous stabilizers for nonlinear systems with uncontrollable unstable linearization," *Syst. Control Lett.*, vol. 42, no. 3, pp. 185–200, 2001.

Haining Sun (M'23), received the B.Eng. degree in mechanical engineering from Shandong University, Jinan, China, in 2017, and the Ph.D. degree in mechanical engineering from Tsinghua University, Beijing, China, in 2022. He is currently with the Singapore Institute of Manufacturing Technology, Singapore. His current research interests include cable-driven robots, vibration control, dynamic control, and force control.

Rongqiao Zhang received the B.S. degree in mechanical engineering from Tsinghua University, Beijing, China, in 2021. He is currently reading a Ph.D in mechanical engineering at Tsinghua University, Beijing, China. His-research interest includes cable driven parallel robots and force control.

Ruihang Ji received the B.S. and Ph.D. degree from Control Science and Engineering, Harbin Institute of Technology, China, in 2016 and 2021. He was a joint Ph.D. student supported by China Scholarship Council with the Department of Electrical and Computer Engineering at National University of Singapore, where he is currently a research fellow. His current research interests include adaptive control and Unmanned Aerial Vehicle.

Xiaoqiang Tang received the Ph.D. degree in mechanical engineering from Tsinghua University, Beijing, China, in 2001. He is currently a Professor with the Department of Mechanical Engineering, Tsinghua University. His research interests include parallel manipulators, robots, and reconfigurable manufacturing technology.

Shuzhi Sam Ge (Fellow, IEEE) received the B.Sc. degree from the Beijing University of Aeronautics and Astronautics, Beijing, China, in 1986, and the Ph.D. degree from the Imperial College London, London, U.K., in 1993.

He is a PI member for Materials Robotic Laboratory, Institute for Functional Intelligent Materials, National University of Singapore, Adjunct SIMTech Fellow, SIMTech, A*Star Institutes, Singapore. He is the Director with the Social Robotics Laboratory of Interactive Digital Media Institute, Singapore and the Centre for Robotics, Chengdu, China, and a Professor with the Department of Electrical and Computer Engineering, National University of Singapore, Singapore, on leave from the School of Computer Science and Engineering, University of Electronic Science and Technology of China, Chengdu. He has co-authored four books and over 300 international journal and conference papers. His current research interests include social robotics, adaptive control, intelligent systems, and artificial intelligence. Dr. Ge is the Editor-in-Chief of the *International Journal of Social Robotics* (Springer). He has served/been serving as an Associate Editor for a number of flagship journals, including the IEEE TRANSACTIONS ON AUTOMATION CONTROL, the IEEE TRANSACTIONS ON CONTROL SYSTEMS TECHNOLOGY, the IEEE TRANSACTIONS ON NEURAL NETWORKS, and *Automatica*. He serves as the President-Elec, Asian Control Association, 2022-2024, and served as Vice President for Technical Activities, 2009-2010, Vice President of Membership Activities, 2011-2012, At IEEE Control Systems Society. He is also a Fellow of IFAC, IET, and SAEng, CAA, AAIA.

Supplemental Material

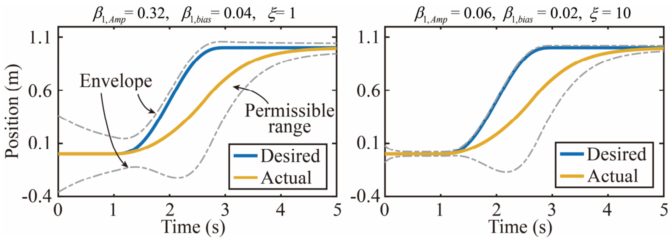

Fig. A1 Influence of $\beta_{k,Amp}$, $\beta_{k,bias}$, and ξ on the envelopes.

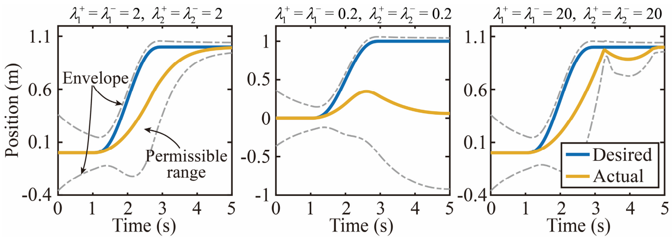

Fig. A2 Influence of λ_1^+, λ_1^-, λ_2^+, and λ_2^- on the envelopes.

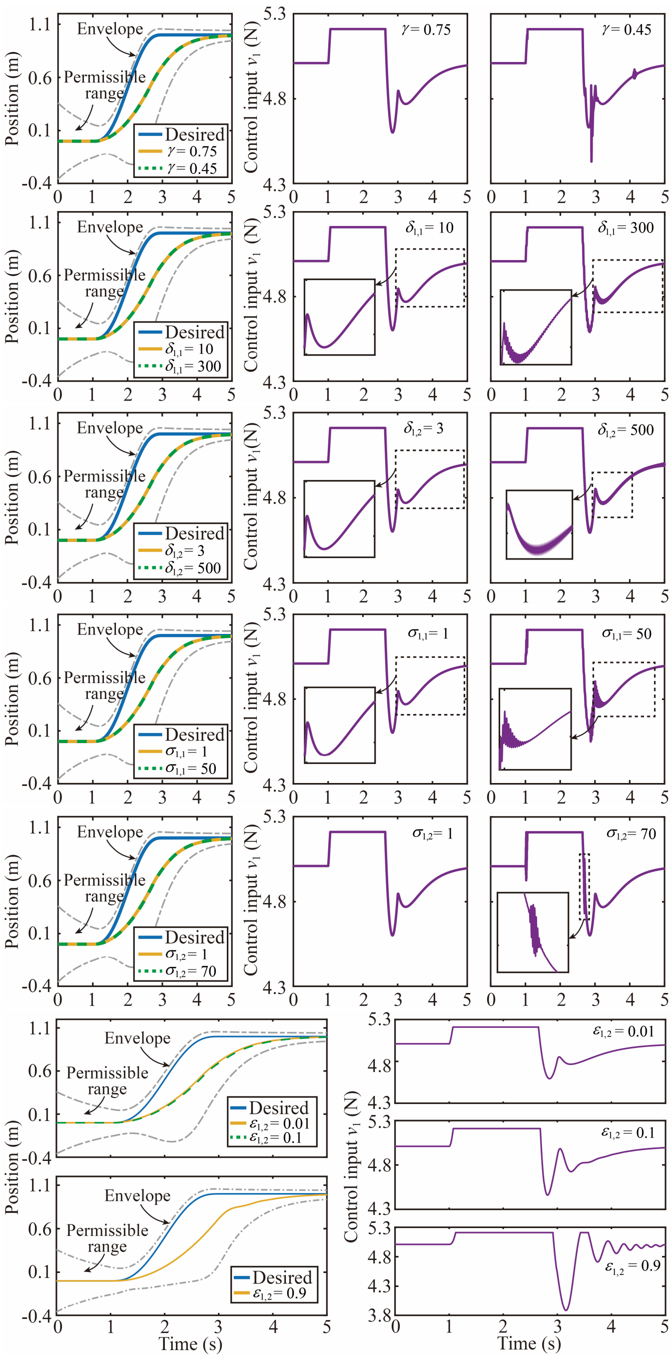

Fig. A3 Influence of γ, $\delta_{k,1}$, $\delta_{k,2}$, $\sigma_{k,1}$, $\sigma_{k,2}$, and $\varepsilon_{k,2}$ on envelopes and control input.